

ORIGINAL RESEARCH

Polarimetric airborne scientific instrument, mark 2, an ice-sounding airborne synthetic aperture radar for subglacial 3D imagery

Álvaro Arenas-Pingarrón¹  | Hugh F. J. Corr¹ | Carl Robinson¹ | Tom A. Jordan¹  | Paul V. Brennan² 

¹British Antarctic Survey, Cambridge, UK

²Department of Electronic and Electrical Engineering, University College London, London, UK

Correspondence

Álvaro Arenas-Pingarrón.
Email: alvnga99@bas.ac.uk

Funding information

Natural Environment Research Council, Grant/Award Numbers: NE/L013444/1, NE/L013770/1; British Antarctic Survey, Grant/Award Numbers: National Capability

Abstract

Polarimetric Airborne Scientific Instrument, mark 2 (PASIN2) is a 150 MHz coherent pulsed radar with the purpose of deep ice sounding for bedrock, subglacial channels and ice-water interface detection in Antarctica. It is designed and operated by the British Antarctic Survey from 2014. With multiple antennas, oriented along and across-track, for transmission and reception, it enables polarimetric 3D estimation of the ice base with a single pass, reducing the gridding density of the survey paths. The off-line data processing stream consists of channel calibration; 2D synthetic aperture radar (SAR) imaging based on back-projection, for along-track and range dimensions; and finally, a direction of arrival estimation (DoA) of the remaining across-track angle, by modifying the non-linear MUSIC algorithm. Calibration flights, during the Antarctic Summer campaigns in 16/17 and 19/20 seasons, assessed and validated the instrument and processing performances. Imaging flights over ice streams and ice shelves close to grounding lines demonstrate the 3D sensing capabilities. By resolving directional ambiguities and accounting for reflector across-track location, the true ice thickness and bed elevation are obtained, thereby removing the error of the usual assumption of vertical DoA, that greatly influence the output of flow models of ice dynamics.

KEYWORDS

airborne radar, array signal processing, direction-of-arrival estimation, MUSIC algorithm, remote sensing by radar, synthetic aperture radar

1 | INTRODUCTION

Polar regions are sensitive to climate change. A source of criticism of global concern is the number of different climate behaviour predictions, which arise from the uncertainties and sparseness of the gridded measurements involved. Ice thickness is one of the key parameters for the elaboration and validation of climate models, because it conditions the ice volume, ice-shelf thinning, flow speed in ice streams, and subglacial channel and crevasse formations. Ice thickness reaches 4.8 and 3 km in Antarctica [1] and the Greenland ice sheet [2] respectively. To meet the challenge, new instruments, processing and

targeted data acquisition campaigns have gained in importance, together with the open-access publication of results. For example, BEDMAP (in 2001) and its update BEDMAP2 (2013) [1], and the BedMachine Antarctica (2020) [3], all as international initiatives with continental ice thickness estimations from measurements collected over the last 50 years; and British Antarctic Survey (BAS) scientists and data managers created an open-access online interface to visualise and download Antarctic aerogeophysical datasets [4], consisting on radar, gravity, and magnetic data collected and processed by BAS.

The first airborne radar campaigns were performed during the '60s. From 1964, the Scott Polar Research Institute (SPRI)

This is an open access article under the terms of the [Creative Commons Attribution](https://creativecommons.org/licenses/by/4.0/) License, which permits use, distribution and reproduction in any medium, provided the original work is properly cited.

© 2023 The Authors. *IET Radar, Sonar & Navigation* published by John Wiley & Sons Ltd on behalf of The Institution of Engineering and Technology.

designed the SPRI Mark II radar [5], with folded dipoles antennas and aiming at a maximum detection depth of 5 km. Airborne 3D-mapping capabilities of the ice base were demonstrated by The Centre for Remote Sensing of Ice Sheets (CRISIS) [6], processing data taken by a Kansas University (KU) airborne radar centred at 150 MHz and with 20 MHz bandwidth [7]. CRISIS also designed a multiband frequency system [8] for altimetry, internal layering, and ice-shelf thickness detection, including the sensor MCoRDS/I for 3D bedrock cartography, at 195 MHz central frequency and 30 MHz bandwidth; and MCoRDS4 [9], at 320 MHz and with 260 MHz bandwidth, using 8 antenna elements in transmission and reception for 3D imagery. The Technical University of Denmark (DTU) developed POLARIS [10], an airborne SAR at 435 MHz with sensitivity to reach up to 4 km thickness, using 8 receivers grouped in 4 sub-apertures for across-track direction of arrival (DoA) estimation [11]. Other ice-penetrating radars are installed in ground vehicles, like the CRISIS instrument at 210 MHz and with 180 MHz bandwidth [12], the first achieving seamless basal 3D-maps.

PASIN2 is the latest evolution of the BAS airborne radar PASIN [13]. It aims to map in 3D the bottom of glaciers, either bedrock or water. PASIN2 was one of the instruments for surveying the Filchner Ice Shelf System in a research framed within the UK Earth System Modelling Strategy, and takes part in other national and international collaborations, like AGAP [14] and PolarGAP [15].

In Section 2 the radar system is described. Section 3 develops the SAR processing and the DoA estimation algorithms. Here is detailed the linearisation and uniformisation of the receiver array, which is non-linear due to aerodynamic constraints, and how this affects the DoA estimations. Calibration and antenna patterns are also presented. Section 4 includes the results for DoA estimation and 3D-mapping, from data collected by BAS in a region of glaciological interest. This section also shows how the non-linear array can be used as a diversity factor for resolving the detection ambiguities. The polarimetric capabilities are currently under study, and thus out of the scope of this paper.

2 | INSTRUMENT DESCRIPTION

PASIN2 is an airborne pulsed SAR at 150 MHz (wavelength $\lambda_0 = 2$ m in vacuum) and 13 MHz bandwidth, mounted in a Twin Otter platform. It can be operated as part of a geophysical suite with additional radars, sensors for magnetic and gravity field detection, lidar, and a camera. Accurate time and positional data are obtained via geodetic GPS.

2.1 | Antennas

PASIN2 has 12 antenna elements: 8 underwing-antennas switching between transmit (TX) and receive (RX) modes, and 4 pod-antennas being RX-only. The 8 TX/RX elements are folded dipoles of length $0.39\lambda_0$, 4 at each side (port and

starboard) and separated by $0.8\lambda_0$. The 4 RX-only are end-loaded printed dipoles within a radome attached to the fuselage, with a separation of $0.5\lambda_0$, and are referred as belly. Belly elements (manufactured by Chelton) are designed to have the same radiation pattern as wing elements. The antenna locations are constrained by the platform certification and frequency band. The 12 elements are independent receivers, whereas the 4 elements in port and starboard arrays are each driven simultaneously (with the same excitation coefficients), hence achieving 24 phase centres (2TX, 12RX), non-unique. The wings, with a slope (dihedral) of $\sigma = 3.5^\circ$, behave as plane reflectors for port and starboard elements, directing the TX pattern of each array towards different directions. The antenna orientation for along-wing (H) or along-track (V) polarisation must be manually changed before taking off, in port and starboard. Figure 1 shows a laser-scanned 3D model of the aircraft and a picture with the folded dipoles under port wing. Folded dipole directivity is 2.15 dBi, plus 3 dB in case of port and starboard elements due to the wing reflector at $\sim\lambda_0/4$, hence 5.15 dBi. In transmission, the 4-elements array add 6 dB to the overall gain, achieving 11.15 dBi. Table 1 lists the main parameters of the system.

2.2 | Transmission and reception

The transmission method is time-division multiplexing with a system pulse repetition frequency (SPRF) of 15.625 kHz, and a receiving window of 64 μ s (full cycle). The maximum number of pre-programmed alternating transmissions is 8, including TX side and pulse type, and are referred as *waveforms*, normally using 5. The transmitted signals are generated with an arbitrary waveform generator (AWG), directly tuning the carrier frequency to 150 MHz. The AWG has two independent outputs, for port and starboard, and each divides into four towards separated low pass filters, high-power amplifiers and the antenna elements. TX and RX modes are controlled by an antenna switch. In reception, after a low pass filter, each channel is digitised at 120 MHz rate (ADC, Pentek 71660 4-channel 16-bit

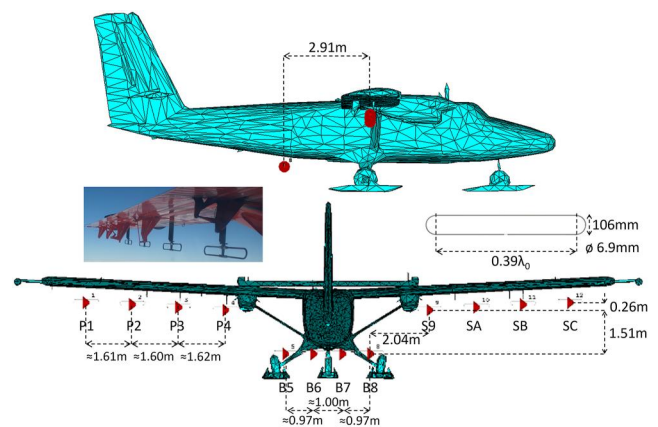


FIGURE 1 Polygonal laser-scanned model of the Twin Otter platform, with the antenna names and relative distances.

TABLE 1 PASIN2 parameters.

Central frequency	150 MHz	f_c
Bandwidth	13 MHz	B_w
Sampling frequency	120 MHz	f_s
Cyclic waveforms (up to 8)	4 μ s port (0)	N_W
	4 μ s starboard (0)	
	4 μ s port (π)	
	4 μ s starboard (π)	
	1 μ s port	
System pulse repetition frequency	15.625 kHz	$SPRF$
Stacking factor	25	N_{ST}
Effective pulse repetition frequency	125	$PRF = SPRF / (N_W N_{ST})$
Transmitters: 4-Element arrays	2 (independent)	TX
Transmitter peak power	4 \times 500 W (16/17)	
	4 \times 1000 W (19/20)	
Transmitter gain	11.15 dBi	
Transmitter 3dB-beamwidth	$\approx 13^\circ$ (across-track)	
Transmitter 10dB-beamwidth	$\approx 25^\circ$ (across-track)	
Receivers: Elements	12 (independent)	RX
Receiver gain	5.15 dBi (wings, 8)	
	2.15 dBi (belly, 4)	
Receiver Doppler beamwidth	$\approx 9^\circ$ (square pixel); $\approx 60^\circ$ (Doppler scattering)	Ω

digitiser on a custom FPGA), and echoes from the same waveform within the transmitted sequence are stacked (summed) with a fixed amount of 25, giving an effective pulse repetition frequency (PRF) of 125 Hz. The resulting signal is stored in one of the three 1 TB units (separated for port, belly, and starboard sections). Assuming a nominal aircraft speed $v_0 = 60$ m/s, for a single waveform (TX side and pulse type), the storage rate per 4-element section is 0.64 GB/km. A quick-look of the radar data is displayed in real-time for assessment by the operators.

The transmitted pulses are chirps with linear frequency modulation. The bandwidth is limited to 13 MHz, with duration of 1 μ s or 4 μ s. To filter common interference and ADC offsets, the 4 μ s-pulses are transmitted in 2 different waveforms: one shifted 180° relative to the other (0- π modulation). In the off-line processing, received signals from both waveforms are subtracted, cancelling the common sources and increasing the SNR by 3 dB, with a coherence interval of 128 μ s, or ~ 8 mm for an aircraft speed v_0 .

The antenna locations and other instrument and processing parameters can be found in the parameter files in the public repository [16].

2.3 | Positioning and attitude data

Global Positioning System (GPS) and Inertial Measurement Unit (IMU) devices are integrated, to obtain geographic coordinates (latitude, longitude, and elevation) and rotation angles (roll, pitch, and yaw), sampled at 10 Hz. A near-infrared scanning lidar (Riegl LMS-Q240i) provides the terrain clearance (distance from radar to surface), with a maximum range of 650 m and 2 mm accuracy.

3 | DATA PROCESSING

After data storing and formatting, processing is performed off-line using Matlab. It consists of range and along-track focussing, channel calibration, free-space direction of arrival (DoA) estimations and 3D-mapping. For the DoA calculations, a single TX array and the 12 RX channels were used in this work. For the DoA, the elevation angle α is zero at nadir (downwards, vertical), positive from port (left) and negative from starboard (right), within $\pm 90^\circ$. From the tip (outboard) antenna of port wing to the tip of starboard, antenna elements are labelled as P1, P2, P3, and P4 for port; B5, B6, B7, and B8 for belly; and S9, SA, SB and SC for starboard (Figure 1).

3.1 | SAR processing

Impinging signals at each receiver are sampled with its ADC at $f_s = 120$ MHz. Since the bandwidth B_w is limited to 13 MHz, the central frequency $f_c = 150$ MHz is shifted unambiguously to 30 MHz after the ADC. The demodulation to baseband (conversion from real to IQ domain) is achieved with a Discrete Fourier Transform (DFT) of the signal, by reassigning its frequencies from the interval between 0 and 60 MHz (up to $f_s/2$) to -30 and 30 MHz, and converting back to time domain.

The propagation media are free space and a homogenous ice layer of refractive index $n_r = 1.78$, whose interface is approximated as *locally* horizontal. Except for the wave refraction at the air-ice interface, the englacial volume to be imaged is well represented by cylindrical coordinates, with the cylinder main axis, radius and angles corresponding, respectively, to the platform direction (along-track), range and elevation angle (across-track). For a single phase-centre of a TX-RX pair, the antenna orientations and the SAR processing do not resolve the across-track angles, resulting in a 2D SAR image with only along-track and range dimensions. In 2D at zero-Doppler the antennas are mainly looking downwards, and the englacial depth is assumed to depend only on the estimated range, despite the locus of possible reflectors with identical range. This incorrect interpretation (with the corresponding topography) justifies a multichannel radar for 3D capabilities. After processing several 2D SAR images, the across-track (elevation) angle is resolved by MUSIC algorithm (Multiple SIngle Classification) [12, 17–19]. Finally, range and elevation angle (polar coordinates) are converted into vertical and horizontal across-track dimensions (Cartesian coordinates).

SAR imaging is performed in range and along-track dimensions. The latter is defined as the vertical projection of the platform trajectory, and hence it is not a straight line. Range focussing is made with a matched filter (compression) according to the chirp parameters, with a group delay error due to propagation lower than 10 ns for 13 MHz bandwidth and a depth of 5 km [20]. Range resolution δ_R in ice depends on the chirp bandwidth and refractive index, as [21].

$$\delta_R = \frac{c_0}{2B_w \cdot n_r} \quad (1)$$

with c_0 the speed light in vacuum, hence $\delta_R \approx 6.5$ m. Along-track resolution (δ_a) is determined by the aircraft speed (v) and the Doppler bandwidth (B_d), which takes the same expression as in homogeneous-medium SAR. For unsquinted symmetrical SAR geometry with full aperture angle Ω [21]

$$B_d = \frac{4v}{\lambda_0} \sin(\Omega/2) \quad (2)$$

$$\delta_a = \frac{v}{B_d} = \frac{\lambda_0}{4\sin(\Omega/2)} \quad (3)$$

Aperture Ω can be limited to have a square pixel resolution in the SAR image. Equalling resolutions Equations (1) and (3) results in $\Omega \approx 9^\circ$ (Table 1). From rough bedrock, clear back-scattering up to $\Omega \approx 60^\circ$ ($\pm 30^\circ$) has been detected.

Back-projection (BP) [22] is chosen as along-track focusing method for its flexibility. This is appropriate for non-straight radar-platform trajectories and for output analysis, to refine the along-track reference functions. Given the set $P_s(k_d, k_a)$ of scatterers (targets) under test, defined by their depth and along-track indexes k_d and k_a , respectively, and the set $P_n(T)$ of TX and RX locations for channel n when the T th pulse was transmitted. The round-trip propagation time from radar to target will correspond to the sample k_r of the range-compressed received signal $a_{c,n}$ for channel n . The incident angle in free space of the wave trajectory is θ_0 , constrained to $|\theta_0| \leq \Omega/2$. BP consists of the coherent integration of samples k_r , from the first pulse (T_F) to last (T_L) in which the target is seen by the radar, with TX and RX locations depending on the rotation angles. The same set of scatterers $P_s(k_d, k_a)$ will be selected for each SAR image. The coherence is achieved by correcting the phase φ of samples k_r , accounting for the propagation delay relative to the phase of shortest path in pulse $T_0(k_d, k_a)$. Hence, output SAR $_n$ is

$$\begin{aligned} \text{SAR}_n(k_d, k_a) &= \sum_{T=T_F}^{T_L} a_{c,n}[k_r(T), T] \\ &\cdot \exp(-j\varphi(P_n(T), P_s(k_d, k_a))) \\ &\cdot \exp(+j\varphi(P_n(T_0), P_s(k_d, k_a))). \end{aligned} \quad (4)$$

The exact propagation delay calculation is a processing bottle neck. Techniques based on small-angle approximations are used to speed the throughput, for either single values or

lower and greater limits followed by an iterative search. The signal path will depend on the relative refractive index and the locations of TX, target and RX, considering the aircraft rotation angles.

3.2 | Calibration

In-flight measurements of TX antenna patterns and relative amplitude, phase and delay (APD) values between receivers are needed to ensure an optimum combination of channels. A flight above the sea surface (with low sea state) near Rothera Station (Adelaide Island, Antarctic Peninsula) while varying the aircraft rotation angles has been used for calibration, as in ref. [23]. The roll angle is defined as positive when the port tip raises above the starboard tip; and the pitch angle is defined as positive when the aircraft nose raises.

Due to the specular reflection of transmitted waves from a calm sea surface, the DoAs are within an extremely narrow beam perpendicular to the sea surface. For any roll angle ρ , according to the conventions in the introduction of Section 3, the main DoA from the sea surface will be zero; instead, if a new reference system is fixed to the aircraft (body-fixed frame axis) its DoA will be $-\rho$. A calibration flight with single polarisation (H) was performed in season 16/17, with the roll varying sinusoidally between -25° and $+25^\circ$, and pitch constrained to within 5° . After range-focussing, the peak location corresponds to the distance from radar to sea surface. The amplitude levels are the product of the TX pattern and the individual RX pattern. As the RX beamwidth is much greater than the TX array factor, the roll variation estimates the TX pattern of port and starboard arrays, and provides the variations between the antenna elements.

Because APD depend on the DoA, the full correction cannot be applied to the radar data, only their mean values. Mean APD values are obtained by first taking as reference the peak response at one of the RX's and TX's. Then, after removing the relative phase and delay due to the rotation angles from the peak response at each receiver, the mean of the remaining APD are the mean calibration values added by the different electronic paths, components and aircraft structure. Mean APD values can be corrected at any processing step in the IQ domain. The compensation effect was verified by comparing the estimated DoA in the roll-varying section of the calibration flight, using the MUSIC algorithm before and after applying the calibration. Before application, there is an offset between the roll angle from the IMU and that obtained from the DoA, together with high noise floor levels; after the compensation, both IMU and estimated roll match. With this method there was also detected a delay of 1 s between the radar timestamp and GPS clock. The mean calibration values are expected to be constant, but if there is any modification from flight to flight in the electronics, the same mean APD values no longer apply. To ensure the internal calibration, a second calibration loop is performed in which the amplitude and phase of *direct* received pulses are measured. These *direct* pulses are of two kinds: 1) coupled pulses from antenna to

antenna without reflecting or scattering from surfaces (water, ice, ...), which happen when the RX is not on the same side of the TX; and 2) breakthrough pulses, leaking within the isolator separating transmission from reception, which occur in RX's on the same side as the TX. Unless a change of polarisation, as the aircraft and antenna locations are invariant the paths of *direct* pulses are constant, therefore a change in the electronics will be detected in the direct echoes. A comparison of the direct responses in the imaging and calibration flights is used to check the mean APD values.

Port and starboard TX radiation patterns are displayed, respectively, in Figure 2a,b, against the elevation angles regarding the body-fixed axis and normalised to the maximum. They include CST Studio Suite simulations with the aircraft 3D model (dash-dotted black), the patterns using the coefficients measured from the breakthrough pulses (dashed black), and the amplitude peak from the range-compressed pulses for all RX channels (solid and dashed colours). In the season 16/17, besides the single-polarisation (H) flight, a polarimetric flight was done with the port section as V, and belly and starboard as H. Then, depending on the combination of TX and RX the patterns represent the co- or cross-polar channels. Due to the wing slopes ($\sigma \approx 3.5^\circ$) the patterns have their maximum at opposite angles. Starboard pattern measurements are broader than expected, which we attribute to the lower amplitude of one radiating element.

Phase deviations from the mean as a function of elevation (roll) angle arise from hull reflections and the wing curvature. These deviations are shown in Figure 3 as the residual phase differences between consecutive channels, measured with the calibration flights of 16/17 (as for Figure 2) and other fully

polarimetric from season 19/20 (but with roll between -10° and $+10^\circ$), after correcting each channel with its corresponding mean calibration phase per season. Figure 3a compares the residual of port TX relative to starboard TX, both in H from 16/17. Apart from the pattern nulls, the linear plots suggest an offset of the phase-centre locations. The residual error at the receivers is expressed as the phase difference between consecutive receivers in Figure 3b, in the single-polarimetric flight of 16/17. Except for an offset, there is an approximated symmetry for analogous channel pairs, and *anti-symmetry* for the elevation angle. The residuals errors of the co-polar receivers in seasons 16/17 and 19/20 are compared in Figure 3c,d, respectively with H (starboard) and V (port). The residuals are similar for both seasons, indicating they are due to the aircraft structure.

The data with calibration results and software to read them and represent as in Figures 2 and 3 are available in the public repositories [16, 24] respectively.

3.3 | DoA estimation

A free-space DoA with across-angle α has a reference column vector s_α with N complex coefficients, according to the TX and RX locations of each channel n , from port (P1) to starboard (SC):

$$s_\alpha = [1 \quad e^{j\phi(P_2, \alpha) - j\phi(P_1, \alpha)} \dots e^{j\phi(P_N, \alpha) - j\phi(P_1, \alpha)}]^T \quad (5)$$

where P1 is taken as reference. After the calibration, amplitude levels are equalised for every channel to have the same level from nadir DoA ($\alpha = 0^\circ$), and hence the coefficients of s_α are approximated only by its phase ϕ .

After the N SAR images Equation (4) of the corresponding N channels are processed, the DoA for a target under test is estimated with MUSIC. The input is the set of N complex values corresponding to the same focused pixels (k_d, k_a) in Equation (4). MUSIC is a high-resolution technique, but because of its non-linear properties it is applied for DoA detection rather than for backscattering level measurements. It is a supervised method, since it requires a number M of DoAs per range bin. To distinguish left from right DoA, M is usually limited to 2 [12], but in some environments only 1 can be found [11]. In cases where the scattering from nadir is strong enough such that its sidelobes leak into other far range bins, M can be 3. By eigenvalue decomposition (ED), Q eigenvectors ($Q > M$) of the correlation matrix from the input data are obtained. The M eigenvectors with highest eigenvalues span the DoA signals subspace \mathcal{S} , whereas the noise subspace \mathcal{I} is spanned with all Q eigenvectors, and hence the dimensions are $\dim(\mathcal{S}) = M$ and $\dim(\mathcal{I}) = Q$. Since eigenvectors are orthogonal, the M vectors $s_\alpha \in \mathcal{S}$ have a zero projection onto the subspace defined by $Q - M$ eigenvectors. The output of MUSIC is the inverse of this projection for all the DOA angles under test, and will be a local maximum for M angles. For a better

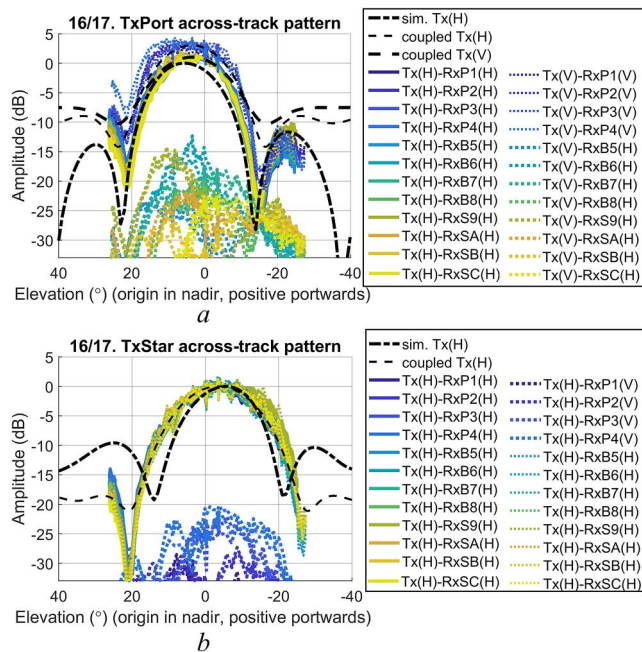


FIGURE 2 Across-track antenna patterns for all the H and V polarisation channels, simulated and from calibration flights. (a) Port and (b) Starboard transmitter arrays.

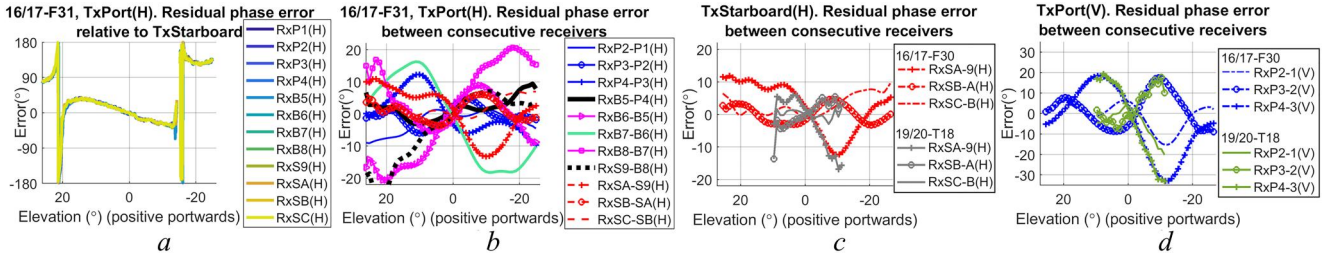


FIGURE 3 Residual phase errors ($^{\circ}$), after correcting average constant phase errors at each receiver and transmitter. (a) Port transmitter array (H) relative to starboard (H), for each receiver, (b) All consecutive receiver (H) pairs, transmitting from port (H), season 16/17, F31 (c) Starboard receiver (H) pairs, transmitting from starboard (H), seasons 16/17 (F30, red) and 19/20 (grey) (d) Port receiver (V) pairs, transmitting from port (V), seasons 16/17 (F30, blue) and 19/20 (green).

estimation of the correlation matrix, N_S along-track pixels (snapshots) around k_a are used. The averaged correlation matrix $R_{S,Q}$ is estimated from the Toeplitz matrices $S_Q(k_d, k_a)$ using the *covariance* method [18] as follows:

$$S_Q(k_d, k_a) = \begin{bmatrix} \text{SAR}_Q & \cdots & \text{SAR}_1 \\ \vdots & \ddots & \vdots \\ \text{SAR}_{2Q-1} & \cdots & \text{SAR}_Q \\ \vdots & \ddots & \vdots \\ \text{SAR}_N & \cdots & \text{SAR}_{N-(Q-1)} \end{bmatrix} \quad (6)$$

$$R_{S,Q}(k_d, k_a) = \frac{1}{N_S} \cdot \sum_{i=k_a-(N_S-1)/2}^{k_a+(N_S-1)/2} S_Q^H(k_d, i) S_Q(k_d, i) \quad (7)$$

with $(^H)$ the transpose conjugate, N_S odd, $0 < M < Q$ and $Q \leq (N+1)/2$, the latter for achieving the number of rows in Equation (6) is greater or equal than Q , and hence S_Q and $R_{S,Q}$ have rank Q . If N cannot ensure $0 < M < Q$, instead of the *covariance* method it is used the *correlation* method [18] (with Q columns)

$$S_Q(k_d, k_a) = \begin{bmatrix} \text{SAR}_1 & & 0 \\ \vdots & \ddots & \\ \vdots & \ddots & \text{SAR}_1 \\ \text{SAR}_N & \ddots & \vdots \\ & \ddots & \vdots \\ 0 & & \text{SAR}_N \end{bmatrix} \quad (8)$$

MUSIC is based on the null dot product of s_{α} and, at least, one of its own eigenvectors $u_{\alpha n}$. But this condition is not generally met for non-uniform arrays, like PASIN2, as analysis of eigenvectors $u_{\alpha n}$ of s_{α} results in

$$u_{\alpha n}^H \cdot s_{\alpha} \neq 0, n = 1, \dots, N \quad (9)$$

To ensure the orthogonality, $u_{\alpha n}$ eigenvectors of s_{α} are obtained by analogy to Equations (6) and (7) and ED, and the one with highest eigenvalue, $u_{\alpha,1}$, will be used as reference instead of s_{α} . Given the Q column eigenvectors v_n of R_S Equation (7), with n ordered in decreasing eigenvalue, MUSIC output is

$$\text{DOA}_{MU}(\alpha, M, Q) = \left(\sum_{n=M+1}^Q |v_n^H \cdot u_{\alpha,1}|^2 \right)^{-1} \quad (10)$$

The greater the $Q - M$ dimensions only associated to the noise subspace I , the more elements to be summed in the denominator of Equation (10), and hence a poorer result when lack of orthogonality. If $\dim(I)$ is reduced to the limit $Q = M + 1$, then

$$\text{DOA}_{MU}(\alpha, M, M+1) = |v_{M+1}^H \cdot u_{\alpha,1}|^{-2} \quad (11)$$

improving the noise floor level without the summation in Equation (10).

After calibration, let the vectors s_{α} be considered as time domain sequences of length N , with $A[n]$ and $\phi[n]$ the amplitude and phase at index n (from port to starboard). $A[n] = 1$ for s_{α} . The normalised phase difference is

$$f_{ins}[n] = \frac{1}{2\pi} (\phi[n] - \phi[n-1]), n = 2, \dots, N \quad (12)$$

analogous to the instantaneous frequency observed after its discrete Fourier Transform, and thus converting the ambiguities into an aliasing problem. MUSIC performance is optimum for uniform arrays, with constant instantaneous frequencies. But PASIN2 array has three geometric particulars: 1) the transition distances from P4 to B5 and B8 to S9 are $1.93\lambda_0$, causing aliasing for any DoA; 2) port, belly and starboard sections are not aligned; and 3) the element distances are uniform within wing ($0.8\lambda_0$) and belly ($0.5\lambda_0$). Hence, the instantaneous frequencies of a DoA are identical only within each section.

PASIN2 is non-uniform except locally. Its capabilities are limited because the aliasing disturbs the overall estimations, above all when $M > 1$, as the relative phases of the M targets strongly affect the correlation Equation (7). Within port section, the DoA interval free of aliasing is $(-35^{\circ}, +42^{\circ})$, full for belly, and $(-42^{\circ}, +35^{\circ})$ for starboard, due to the element distances and the wing slopes. This is shown in Figure 4, with the normalised phase differences Equation (12) of the expected PASIN2 coefficients of each RX, according to their relative location and without calibration errors. The differences are between consecutive RX channels, from P1 (port tip) to SC (starboard tip), for the DoA $0^{\circ}, \pm 13^{\circ}, \pm 28^{\circ}$ and $\pm 34^{\circ}$. The

horizontal axis with the RX corresponds to the n th element in Equation (12), so f_{ins} [2] is indexed at P2. Green region is aliasing-free, within the interval $[-0.5, 0.5]$, and red are aliasing regions, to be wrapped into the green ones. Figure 4a plots the results before aliasing, showing the strong phase variations in the transitions from P4 to B5 (index B5) and from B8 to S9 (index S9). Figure 5a is the result after aliasing, with the instantaneous frequencies in red regions wrapped into the green ones. To avoid the transitional aliasing, the DoA beamwidth using all PASIN2 RX's (and single TX) is reduced to $(-13^\circ, +13^\circ)$.

The mean and standard deviation of the phase differences (12) can be related to the spectral centroid and bandwidth. The eigenvector with the highest eigenvalue, $u_{\alpha,1}$, has nearly zero bandwidth, so it is well represented by a constant phase derivative (like a fundamental *tone*), and its centroid approaches the mean of the phase difference of s_α . The remaining $u_{\alpha,2}$ to $u_{\alpha,N}$ have different centroids and non-zero bandwidths. This justifies using $u_{\alpha,1}$ in Equations (10) and (11). To optimise MUSIC, s_α should describe a *tone*, because s_α would be equal to $u_{\alpha,1}$. Hence, a pre-conditioning of the SAR coefficients Equation (4) must be done before the DoA estimations, to transform the instantaneous frequencies for each DoA into a *tone*, such that PASIN2 resembles a uniform array. The uniformisation is performed with matrix algebra, with identical operations for any DoA. The new set of SAR coefficients increases the beamwidth free of aliasing.

3.4 | PASIN2 uniformisation

Let the original PASIN2 array samples from the SAR images (4) be stored in a row-matrix C_{PSAR} with N channels

$$C_{\text{PSAR}} = [\text{SAR}_1 \quad \cdots \quad \text{SAR}_N] \quad (13)$$

a row-vector W_{DoA} with N_D complex weights, one for each possible DoA α_n (within a beamwidth), with a maximum of M non-zero weights; and a matrix C_P with the reference N complex coefficients in Equation (5) for each of the N_D angles α_n

$$C_P = [s_{\alpha_1} \quad \cdots \quad s_{\alpha_{N_D}}]^T \quad (14)$$

Then, C_{PSAR} can be represented by

$$C_{\text{PSAR}} = W_{\text{DoA}} \cdot C_P \quad (15)$$

The two transitions between sections (port-belly and belly-starboard) can be smoothed. This is done by adding a constant phase ϕ_B in belly channel coefficients, linearly depending on aircraft pitch angle Π . Because belly section is lower than wing sections, the phase differences at both transitions have opposite sign (Figure 4a), making possible the phase offset. Its mean value for a DoA interval $[-45^\circ, +45^\circ]$ and pitch $[-8^\circ, +8^\circ]$ is

$$\phi_B(\Pi) \approx -245^\circ - 9.2 \cdot \Pi(^{\circ}) \quad (16)$$

Figures 4b and 5b represent the case after smoothing the transitions by adding the phase ϕ_B to belly channels, widening the unambiguous DoA beamwidth to $(-28^\circ, +28^\circ)$ because the transitions are within the green region. The smoothing function is represented by a diagonal matrix M_S , whose elements are zero for port and starboard channels, and a complex exponential with phase ϕ_B for belly.

The wing slopes σ shift the instantaneous frequencies by an offset regarding a horizontal array: positive in port wing and

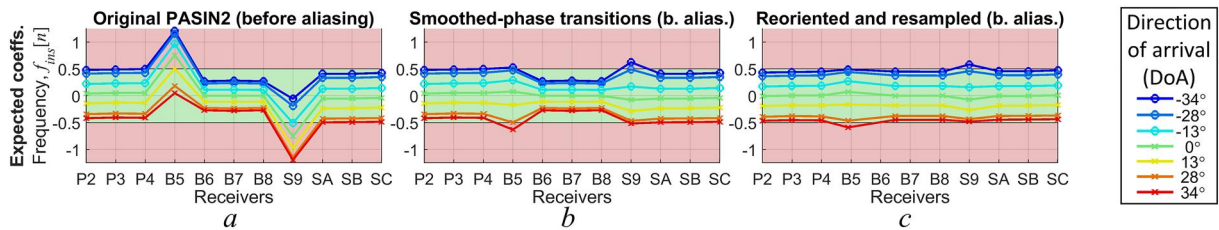


FIGURE 4 Normalised phase difference (frequency) before aliasing, of a receiver relative to the preceding element, from P2 to SC, for several key DoA (legend). Regions without (green) and with (red) aliasing are shown. (a) Original PASIN2, (b) After smoothing transitions P4-B5 and B8-S9, (c) After smoothing, reorienting wing receivers and resampling belly receivers.

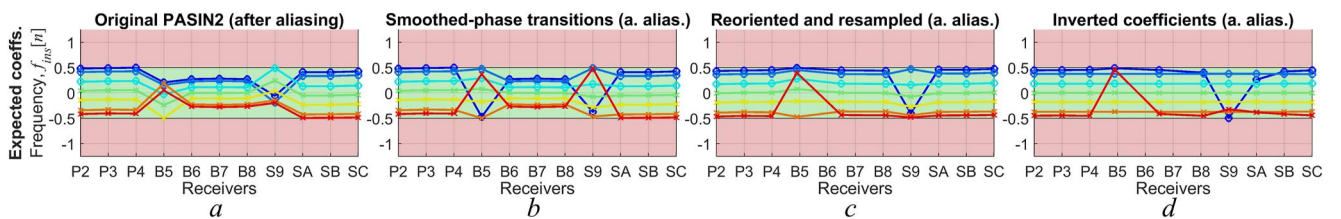


FIGURE 5 Normalised phase difference (frequency) after aliasing. (a–c) Same descriptions as Figure 4. (d) After smoothing, reorienting, resampling and inverting coefficients for approximating flat phase differences.

negative in starboard (Figure 4). By approximating the offset within a section as constant for any DoA, the wing slope is reoriented by applying a diagonal matrix M_{REO} to the channel samples. The main diagonal is the vector m_{REO} , with complex exponentials with linear phase: decreasing for port section, constant for belly and increasing for starboard with $m_{\text{REO}} [4] = m_{\text{REO}} [5] = m_{\text{REO}} [8] = m_{\text{REO}} [9]$ for guaranteeing that the transitions are not affected.

$$m_{\text{REO}}[n] = \begin{cases} \exp(-j2\pi \cdot \sigma \cdot (n-1)), & n = 1, \dots, 4 \\ \exp(-j2\pi \cdot \sigma \cdot 3), & n = 5, \dots, 8 \\ \exp(j2\pi \cdot \sigma \cdot (n-12)), & n = 9, \dots, 12 \end{cases} \quad (17)$$

The separation of belly elements ($0.5\lambda_0$) is shorter than those of the wing sections ($0.8\lambda_0$). Therefore the instantaneous frequencies of the belly are scaled by factor $0.5/0.8 = 0.625$, similar to bandwidth compression. To conform the belly elements to an array of $0.8\lambda_0$ separation, a resampling of s_α or C_{PSAR} is done by subsampling the four coefficients of the belly section with a factor $0.8/0.5 = 1.6$. For this, an interpolation based on Legendre polynomials [25] is used because: 1) the polynomial coefficients depend only on the sampling points (regardless of any DoA combination); and 2) the final scale of the polynomials depends linearly on the weights at each channel (additive property). Let $n = 1, 2, \dots, N$ be the sampling points, with 5–8 corresponding to belly section (B5 to B8) and 6.5 its centre. For a subsampling of factor 1.6, the query points m are 4.9, 6.5 and 8.1, and hence channels P4, B5, B6, B7, B8, and S9 are used for the interpolation. Due to the subsampling, the number of belly coefficients is reduced from 4 to 3, with port and starboard coefficients unaltered. Then, the cost is to reduce from 12 to 11 the number N of coefficients for DoA estimation. The interpolated values at points m are

$$\text{SAR}_m = \sum_{n=4}^9 \text{SAR}_n \cdot f_n(m), f_n(m) = \prod_{k=4, k \neq n}^9 \frac{m-k}{n-k} \quad (18)$$

with $f_n(m)$ degree-5 polynomials on m . Let M_{LEG} be a matrix with the evaluated Legendre polynomials

$$M_{\text{LEG}} = \begin{bmatrix} f_4(4.9) & f_4(6.5) & f_4(8.1) \\ \vdots & \vdots & \vdots \\ f_9(4.9) & f_9(6.5) & f_9(8.1) \end{bmatrix} \quad (19)$$

with I_n and Z_n , respectively, identity and zero matrices of size n , the resampling matrix M_{RES} is

$$M_{\text{RES}} = \begin{bmatrix} I_4 & Z_3 & Z_4 \\ Z_4 & M_{\text{LEG}} & Z_4 \\ Z_4 & Z_3 & I_4 \end{bmatrix} \quad (20)$$

After the smoothing (M_S), Figures 4c and 5c are the frequencies when reorienting (M_{REO}) and resampling (M_{RES}):

belly locations are relocated to 4.9, 6.5, and 8.1, and instantaneous frequencies are equalised and straightened.

PASIN2 coefficients C_P (14) are approximated to a uniform array with the product M_T of the previous matrices as

$$M_T = M_S \cdot M_{\text{REO}} \cdot M_{\text{RES}} \quad (21)$$

such that the transformed coefficients C_T are

$$C_T = C_P \cdot M_T \quad (22)$$

There are phase variations that are not well approximated by a constant offset or a scaling factor, and thus were not included in M_T : 1) the residual instantaneous frequency in the transitions, seen in Figure 5c; and 2) the varying phase calibration errors (Figure 4) depending on both DoA and channel. Hence, M_T transformation by its own does not make C_T corresponds to a uniform array C_U with $0.8\lambda_0$ spacing. With the same weighting matrix W_{DoA} as in Equation (15), the uniform array coefficients C_U would produce the SAR matrix C_{USAR} as

$$C_{\text{USAR}} = W_{\text{DoA}} \cdot C_U \quad (23)$$

After the transformation M_T , the goal is to get a matrix M_I to invert the PASIN2 SAR matrix C_{PSAR} Equation (15) to the equivalent uniform C_{USAR} . By using Equations (15) and (23), it follows:

$$\begin{aligned} C_{\text{PSAR}} M_T M_I &= C_{\text{USAR}} \\ W_{\text{DoA}} C_P M_T M_I &= W_{\text{DoA}} C_U \end{aligned} \quad (24)$$

From Equation (24), M_I is solved by the pseudoinverse (\dagger), as

$$M_I = (C_P M_T)^\dagger \cdot C_U \quad (25)$$

The results after inversion are in Figure 5d. The phase differences are straightened into horizontal lines, describing pure tones in a uniform array. For the pseudoinverse operation, the product $C_P M_T$ was constrained to $\pm 30^\circ$, to ensure a stable behaviour of M_I within these DoA, so DoA $\pm 34^\circ$ still present variations in the transitions. Limiting $C_P M_T$ beyond $\pm 30^\circ$ makes that M_I straightens greater DoA, but at the cost of worsening lower DoA. Smoothing, reorientation, resampling and inversion only affect SAR_n and s_α coefficients, without modifying the MUSIC procedure. The matrix elements in Equation (6) can be obtained from the original SAR images, or after applying on C_{PSAR} Equation (13) any of the operations included in M_T Equation (21) and inversion M_I Equation (25). The eigenvector $u_{\alpha,1}$ (the main associated to s_α) is obtained after an analogous procedure, that is, applying on s_α^T operators M_T, M_I , Equations (6) and (7) and ED. Since for a pure DoA in a uniform array the reference signal and the first eigenvector coincide, the reference is already orthogonal to the rest of eigenvectors and can be used directly without Equations (6) and (7) and ED. This happens after applying the inversion matrix M_I , because the new coefficients are the best approach to the uniform array (with $0.8\lambda_0$ spacing).

The validation of MUSIC and uniformisation is done with the calibration data above the sea surface. Assuming the reference system is fixed in the aircraft, the roll rotation makes an instantaneous varying DoA. The input for assessing MUSIC is obtained by overlapping multiple raw data, range-compressed or SAR image sections, previously compensating their different terrain clearance (to match the range location) and the pitch angles (to correct the phase variations). This results in data equivalent to simultaneous multiple DoA. Three range-profiles from the single-polarisation calibration flight in season 16/17 (Section 3.2), at locations with roll angles -1.6° , -24.6° and $+7.6^\circ$, were added to obtain $M = 3$ DoA from the opposite angles $+1.6^\circ$, $+24.6^\circ$, and -7.6° . The estimations from a single snapshot ($N_S = 1$) are displayed in Figure 6, in images with a normalised scale in dB (coloured), testing the DoA from -50° to $+50^\circ$ in the horizontal dimension. DoA $+1.6^\circ$ was corrected in amplitude and phase regarding the other two components, to be 20 dB greater and have a relative phase from -180° to 180° , shown along the vertical axes. The amplitude and phase of the other two components are equal. Random noise with Gaussian distribution was added, with SNR = 0 dB regarding the signals at $+24.6^\circ$ and -7.6° . The expected DoA are marked by dashed vertical lines. Results from left to right columns show the data pre-conditioning:

original PASIN2 coefficients (left column); after smoothed transitions (middle) with M_S from Equation (16); and after reorienting and resampling (right), with M_{REO} from Equation (17) and M_{RES} Equation (20). In all cases, $M = 3$ and $Q = M+2 = 5$. Figure 7 is after inversion with M_I Equation (25). Figure 8a is with $Q = 6$, and Figure 8b,c with $Q = 4$, all after inversion. Because the smoothing M_S is a square diagonal matrix, it is invertible. Thus, if M_{RES} is not applied, M_I inverts M_S and Figure 7a,b are equal. Estimations improve when inverting the coefficients to obtain the best approximation to uniform array, regardless the application of any transformation matrix. In general, the results are more accurate after resampling and inverting (Figures 7c and 8c), and the noise floor level is lower with $Q = M + 1$ (Figure 8b,c). Due to imperfect inversions of coefficients, the phase errors in a DoA signal might cause false detections, more probably when the signal has an amplitude greater than the others, because its phase error differences can have greater weight regarding the other DoA, and hence be interpreted by MUSIC as an additional DoA. The more similar the amplitude levels, the more reliable the estimations. In the case of a dominant signal (due to the TX antenna patterns), the number M of expected DoA can be incremented in one, to account for the phase errors. This justifies a set of estimations with different M and Q

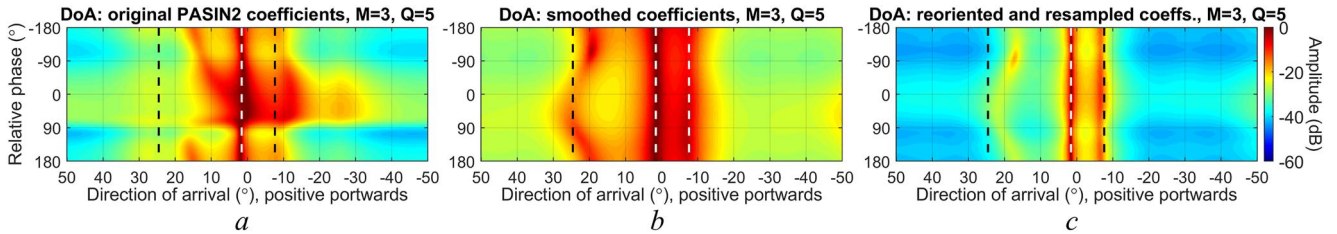


FIGURE 6 DoA estimations (horizontal) with MUSIC (dB, normalised) of $M = 3$ overlapped SAR along-track locations with roll -1.6° (SNR = 20 dB), -24.6° (0 dB) and $+7.6^\circ$ (0 dB). Vertical dimension is the phase of DoA $+1.6^\circ$ relative to DoAs $+24.6^\circ$ and -7.6° . (a) Original PASIN2, (b) After transition smoothing, (c) After smoothing, reorienting and resampling.

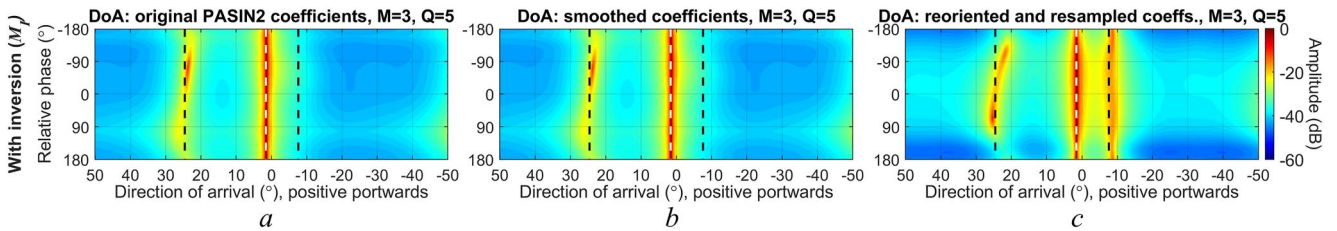


FIGURE 7 DoA estimations with MUSIC, with the same descriptions as Figure 6, but after inverting coefficients for approximating flat phase differences.

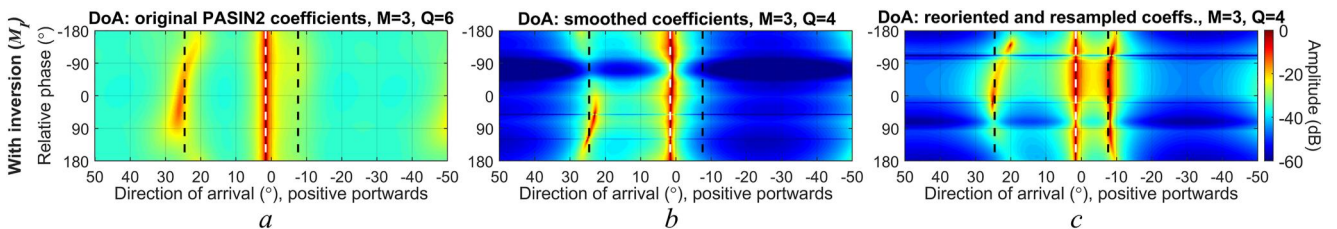


FIGURE 8 DoA estimations with MUSIC, with the same descriptions as Figure 7, but with (a) $Q = 6$, (b) $Q = 4$, and (c) $Q = 4$.

values, from which the final DoA will be estimated. The signal with highest amplitude was always accurately detected.

3.5 | DoA averaging

A DoA estimation ($M \geq 1$) is obtained from the combination of antennas and parameters. A receiver can fail or be poorly calibrated, but if the DoA estimation is performed with the whole PASIN2 array, the effect of this one element is greatly diminished. The combination can be built not only from the full RX-array, but also by consecutive pairs [26], triplets, quartets etc. From a set of estimations at each location (k_d, k_a) Equation (4), the weighted-mean and standard deviation improve the final DoA and evaluate its reliability. For a set of antenna combinations and parameters, prominent scatterers have DoA with lower standard deviations than those from clutter or noise samples. The locations with standard deviation above a threshold can be discarded. A binary classification based on this threshold offers a powerful solution for the automatic detection of bedrock, ice-shelf base and englacial crevasses.

A single RX can be assessed with the several DoAs from the RX-combinations containing it. If for each single DoA the histogram of its deviation relative to the averaged DoA is calculated, those histograms including the faulty RX will be biased regarding others. This assessment also adjusts the calibration phases: if the receiver RX_i is not properly calibrated but its closer neighbours are tuned, DoA estimations from pairs $RX_{i-1}RX_i$ and RX_iRX_{i+1} will have opposite bias in the histograms, whereas other pairs will be unbiased. Similarly, RX-quartets can calibrate port, belly and starboard sections.

4 | RESULTS

The aforementioned methods were applied to data collected during the 2016/17 Austral summer. The flight lines selected are over the Recovery Ice Stream near the grounding line (GL) [27], shown in Figure 9 with Quantarctica [28], a QGIS package developed by the Norwegian Polar Institute. The GL is the climatically sensitive border region where the glacial ice detaches from the ground (bedrock) and starts floating [27], displayed in Figure 9a, from Bedmap2 [1]. Ice streams are fast-

flowing glaciers, driving the continental ice towards the sea. The surface flow speed, obtained with spaceborne interferometric SAR from the MEaSUREs Programme [29, 30], is shown in Figure 9b in $\text{m}\cdot\text{yr}^{-1}$.

The two processed flight tracks are plotted in Figure 9: a section of F07 (black), approximately along-flow of the ice stream and crosses the GL; and a section of F11 (red), almost perpendicular to F07. A *trace* is a period of 200 ms, used as the along-track time units of each track. In Figure 9 the traces are shown as *kilotraces*, shortened as *k*: for F07, the section covers from 71 k to 76 k, and for F11 is from 3 k to 4 k. With an aircraft speed of 55 m/s, a kilotraces corresponds to 11 km.

The presented SAR images and DoA estimations are available in the public repository [24], and the picked basal interface without 3D processing in [4, 31].

4.1 | Ensemble DoA estimation

The SAR image and DoA estimations of a subsection of F07 upstream of the GL are included in Figure 10, with port as TX. The horizontal and vertical axes represent the along-track (from 71 k to 73.15k) and the *equivalent depth* (from -0.18 to 2 km, negative above the surface). The equivalent depth (Eqd) is the depth after incorrectly assuming the echo delay is for vertical DoA. This is the assumed depth from the SAR images (4), now corrected after the DoA is determined and projected. The SAR image (dB) is in Figure 10a, with SC (tip starboard) antenna as RX. The air/ice interface is located at zero Eqd. Until trace 71.5 k, the bed elevation is nearly constant at Eqd 1.25 km, subsiding downstream, but with an unfolding at 71.7 k and 1.4 km. From trace 72.2 k the bed is again found at 1.8 km, slightly rising 70 m, except between traces 72.3 k and 72.5 k, where it is undetected.

The DoA determined from the 12 RX antennas is shown in Figure 10b, with DoA ranging from -30° (starboard) to $+30^\circ$ (port). The estimation parameters from Section 3.3 are $M = 1$ (single DoA) and $Q = M + 1 = 2$, thus corresponding to (11). The DoA of the bed impings from port (DoA > 0) in the shallower Eqd and from starboard (DoA < 0) in the deeper Eqd, until trace 71.3 k, where the DoA is reversed. This means the across-track slope changes its sign. The receding bed is detected with an increasing DoA from port until 71.8 k, but the unfolding at 71.7 k is from starboard at its shallowest Eqd.

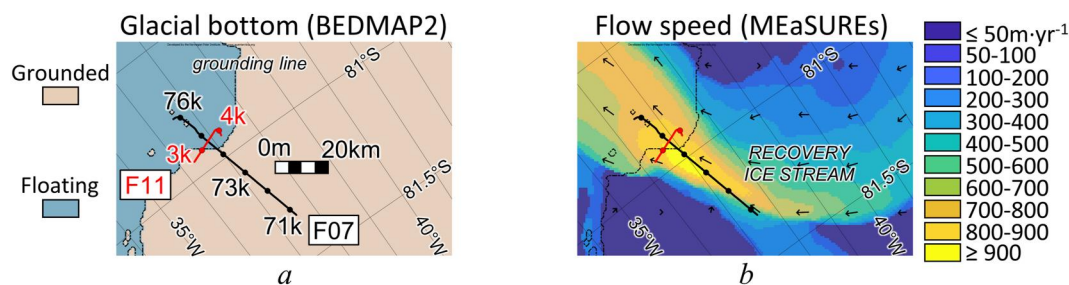


FIGURE 9 Surveyed regions with flight tracks F07 (black) and F11 (red). Maps available from Quantarctica software [28]. (a) Grounded and floating ice, from Bedmap2 project [1], (b) Flow speed ($\text{m}\cdot\text{yr}^{-1}$), from MEaSUREs programme [29, 30].

A weighted average DoA is detailed in Figure 10c, after combining 6 DoA estimations: 4, from the two consecutive triplets of receivers of port (P1-P3 and P2-P4, Figure 1) and starboard (S9-SB and SA-SC); plus 2, from each one quartet of port (P1-P4) and starboard (S9-SC) sections. Belly antennas were not included because of greater clutter. For the averaging, the weight of each group is the number of receivers minus one: 2 for each triplet, and 3 for each quartet. The total weight is $2 \cdot 4 + 3 \cdot 2 = 14$, and the weight percentage of each triplet and quartet is 14.3% and 21.4%. Figure 10b,c show similar results in the locations with detected bed in the SAR image, but clearly different in the englacial (inner) ice. This is due to the reflections from englacial volumetric clutter, and the off-nadir surface and shallow crevasses, whose incoherence is increased by the different sub-array orientations. The standard deviation (std.) of the ensemble DoA estimation is in Figure 11a, with very low values at bed locations. A std. threshold of 5° filters out those locations that do not correspond to the bed, obtaining a binary mask. This is represented in Figure 11b, with the same averaged DoA as in Figure 10c but with the rejected locations masked in white. The initial mask was processed with morphological operations such as opening and closing, to avoid single pixels and unconnected areas.

The number of impinging signals per pixel was $M = 1$. This decision was verified by the histogram of the DoA deviations regarding its ensemble average. The histograms are plotted in Figure 11c, with solid line for $M = 1$ and dashed for $M = 2$, for those locations in Figure 11b at Eqd below 1 km. When $M = 2$, one DoA impings from port and the other from starboard, the latter presented here (from port the histograms were inferior). For both cases, the average DoA was calculated with 7 estimations: 4, from the two consecutive triplets of port and starboard receivers; plus 2, from each one quartet of port and starboard; plus 1, with the full array (of 12 RX, including belly). The black curves correspond to the DoA from the full array, and the grey to the triplets and quartets. For $M = 1$ the full array and small groups estimations were less biased than for $M = 2$, thus preferring $M = 1$. This decision method presents two problems: it is qualitative, and it has local scope. In this case, the increased clutter of the belly antennas broadened and skewed the histograms.

4.2 | DoA aliasing

DoA estimations obtained with the wing receivers may contain aliasing. This is due to the distance between its elements

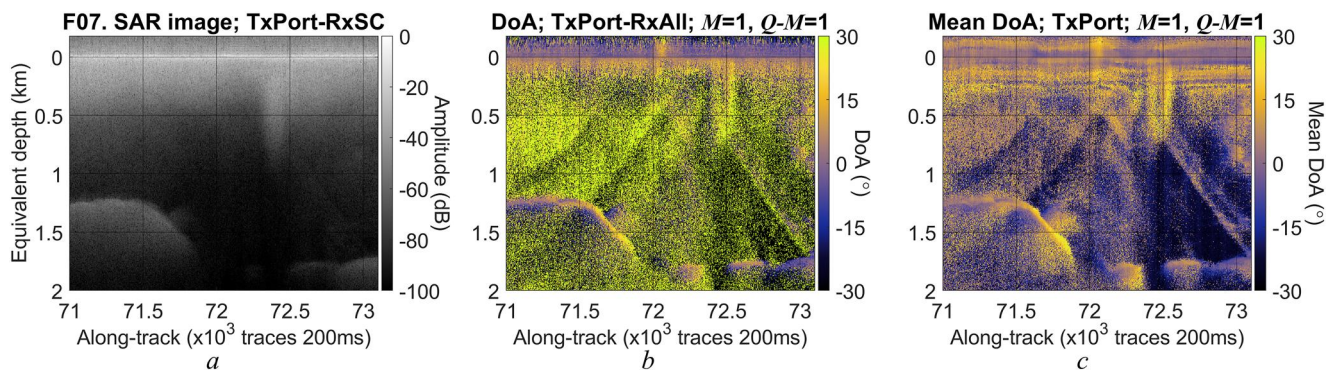


FIGURE 10 Flight F07 processing, between traces 71 k and 73 k and equivalent depth down to 2 km. (a) SAR image (dB, normalised), (b) DoA ($^\circ$, positive portwards) transmitting from port and receiving with the full array, (c) Ensemble mean DoA determined from the triplets and quartets of port and starboard receivers.

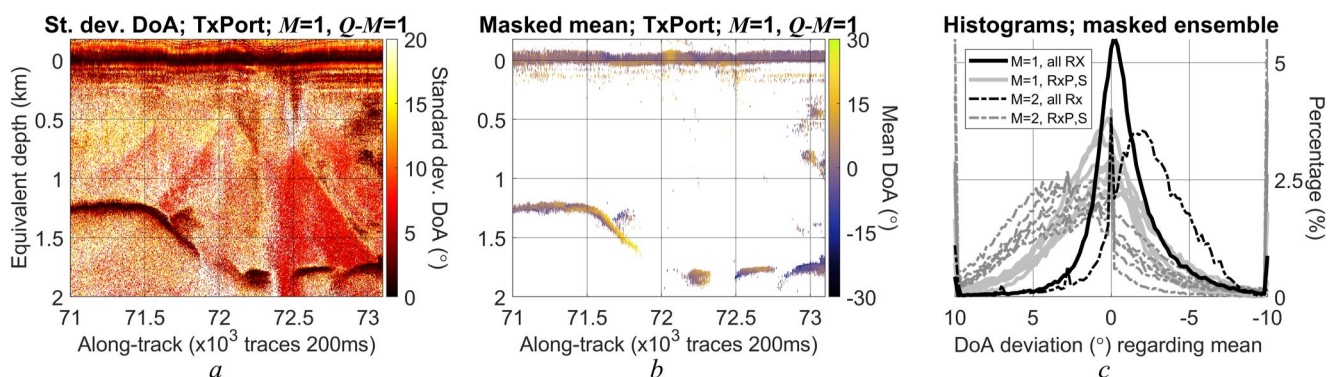


FIGURE 11 F07 processing within the same limits as Figure 10. (a) Ensemble standard deviation DoA ($^\circ$) with estimations as Figure 10c, (b) Mean DoA of Figure 10c with standard deviation lower than 5° , (c) Histograms (%) of DoA ($^\circ$) regarding the means with $M = 1$ (solid) and $M = 2$ (dashed), for estimations with all (black) and port and starboard receivers (grey).

($0.8\lambda_0$), setting a detection limit of $\pm 38.5^\circ$ regarding the across-track direction perpendicular to the wing. However, to account for the non-uniform PASIN2 full array, the processing of Section 3.4 reduces the beamwidth to $\pm 34^\circ$. The wing arrays steer to opposite angles in port and starboard (Figure 1), which improves the across-track detection width, and prevents a null in the antenna pattern from at least one TX array. Belly elements ($0.5\lambda_0$) offer a theoretical full beamwidth detection. For DoA exceeding the detection width, aliasing will occur. The RX-array diversity by comparing DoA estimations from wing and from belly arrays, allows a check for aliasing, similarly to radars with PRF diversity.

Aliasing is observed in the flight F07, between traces 74 k and 76 k. The SAR image (dB) is in Figure 12a, with starboard transmitter and SC receiver. The horizontal and vertical axes are the along-track (kilotraces) and the Eqd (km); the black and white vertical strip is at trace 74.71 k, where F07 crosses perpendicular to F11. This section is over the ice-shelf (floating ice still attached to the ice sheet), within which intense basal melting incises deep channels [32]. These basal channels are prominent scatterers detected in the SAR image. The weighted average DoA from the belly RX-section is in Figure 12b, with 7 estimations from its 3 pairs, 2 triplets and one quartet; and in Figure 12c from the starboard RX-

section, again with its 7 estimations. With the belly section, a basal channel is detected in Figure 12b within DoA -35° and -40° (starboard), ascending from 1.8 to 1.1 km until trace 75 k. Because these angles are out of the unambiguous beamwidth of the wing sections, in Figure 12c the ensemble DoA is aliased and estimated to be from the other side of the aircraft at 30° (port) at trace 74.5 k. The resultant DoA can be close to 0° due to the averaging of aliased and underestimated DoA, like around trace 74.75 k. Other DoA not near the extreme values are comparably measured by both RX-arrays.

4.3 | 3D-mapping

The true depth and geographic locations are found from the Eqd and DoA estimations. After the geometrical corrections [6] that assume a locally flat air/ice interface in the horizontal across-track dimension, the true depth is located along this dimension for the 3D-mapping.

The procedure is evaluated by mapping the depth profile in track F07 at the trace perpendicular (74.71 k) to F11, seen in Figures 9 and 12 (dashed vertical). These track sections are oriented with an 85° difference (crossing at 74.704 k), and

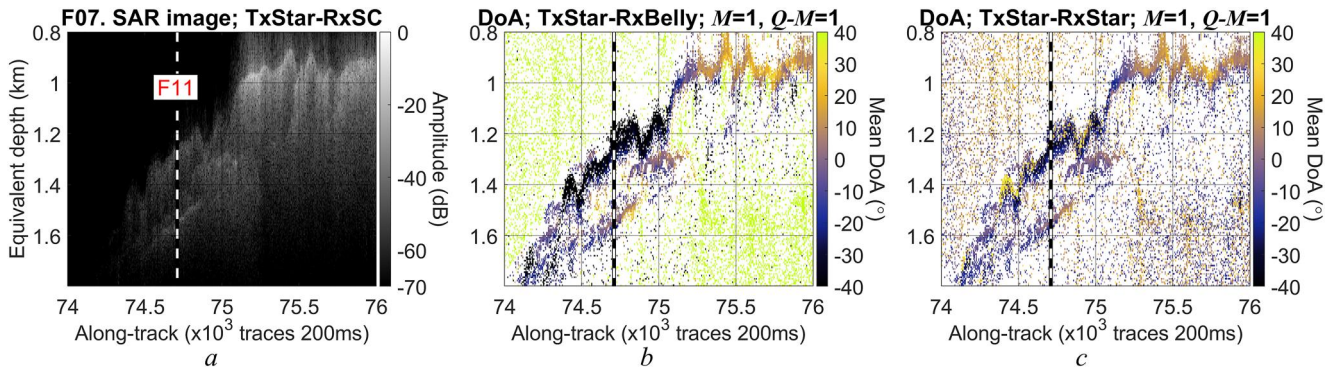


FIGURE 12 F07 processing, between traces 74 k and 76 k with equivalent depth from 0.8 to 1.8 km. (a) SAR image (dB), with trace perpendicular to F11 (dashed), (b) DoA ($^\circ$, positive portwards) transmitting from starboard and receiving from belly array, (c) DoA receiving from starboard array, with aliasing at trace 74.5 k and equivalent depth 1.4 km.

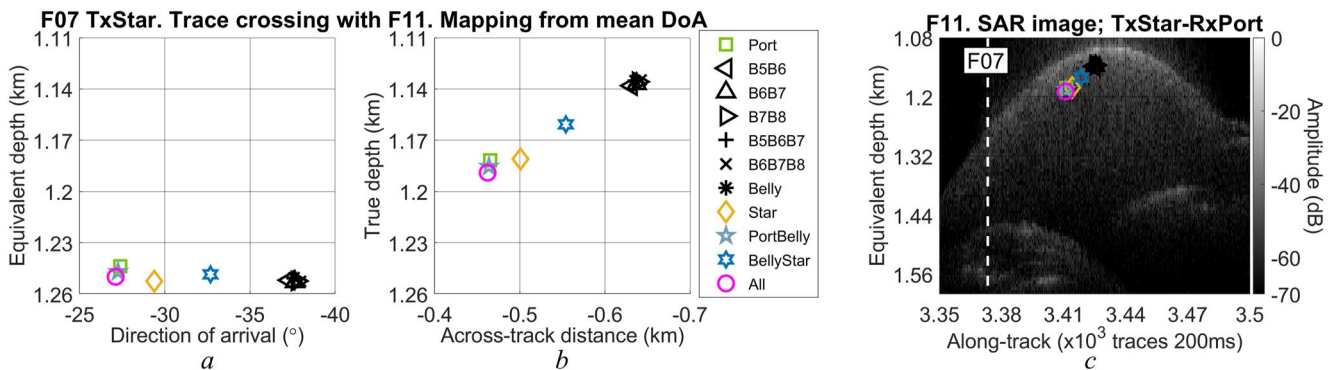


FIGURE 13 3D-mapping from F07 compared to F11 SAR profile. (a) Equivalent depth (km) and DoA ($^\circ$, starboard) of shallowest channel of Figure 12 at trace perpendicular to F11, from several receiver groups (markers), (b) 3D-mappings as true depth (km) and across-track (km), (c) F11 SAR image (dB), with the 3D-mappings of F07 and its crossing trace (dashed).

the 3D locations derived from F07 should match with the detection from the SAR image of F11. The basal echoes correspond to the subglacial channels, which are along-flow features: oriented along-track for F07 and across-track for F11. For F07 at the crossing trace with F11, the averaged Eqd and DoA estimations of the shallowest channel in Figure 12b are plotted in Figure 13a, with the DoA along abscises and the Eqd (km) along ordinates, for several receiver combinations made up by triplets, quartets, octets and full receiver array (see marker legend). Due to the large DoA angle from starboard direction, observations from belly elements (triangles and non-polygonal markers) at -37.5° are valid, whereas as detailed in Section 4.2 those with wing receivers are aliased. The true depth (km) and across-track distance (km, negative towards starboard) are in Figure 13b, with the belly receivers showing a correction of -9% from Eqd (1.25 km) to true depth (1.135 km). The corrections are on the SAR image of F11 in Figure 13c, after accounting for the aircraft speed and the track orientation of 85° . In the SAR image, the apex of the shallowest hyperbola-like feature is found at Eqd 1.1 km, and thus with the belly elements the depth error is 35 m. The tails of the hyperbola are not residuals of the apex SAR-processing, but to the across-track off-nadir echoes from the subglacial channel. The crossing with F07 is marked as a vertical line. Between traces 3.38 k and 3.41 k, the prominent scatterings from Eqd 1.44–1.58 km are also observed in F07 in Figure 12b, between Eqd 1.5 and 1.6 km, with a DoA confined to a few degrees from starboard.

5 | CONCLUSIONS

The airborne ice-sounding SAR system PASIN2 has been presented. Designed for glaciologic surveys, it aims to map in 3D the true basal topography beneath the Antarctic glaciers. The true ice thickness and bedrock relief are critical in sensitive regions for predicting the ice dynamics. PASIN2 consists of a non-uniform array of 12 antennas, which requires calibration to account for the amplitude and phase imbalances of the antenna coefficients due to multipath reflections on aircraft fuselage. For 3D-mapping, the across-track direction of arrival of the received signals is estimated by the MUSIC algorithm. Because MUSIC performance is maximised for uniformly distributed arrays, a pre-processing procedure for obtaining an equivalent uniform array was detailed, which improves outputs. A strategy for identifying the basal interfaces, verification of reflector location and assessment of the receivers has been presented. Primarily, we use the mean and variance as descriptive statistics of ensemble estimations from several antenna combinations. The diversity of the array sections has been shown to offer a great advantage for detecting glaciological features. PASIN2 procedures were validated by comparing nadir and off-nadir scatterers, with perpendicular flights above the Recovery Ice Stream. The next step is the design and assessment of polarimetric surveys.

AUTHOR CONTRIBUTIONS

Álvaro Arenas-Pingarrón: Conceptualisation; Data curation; Formal analysis; Investigation; Methodology; Software; Validation; Visualisation; Writing-original draft. **Hugh F. J. Corr:** Conceptualisation; Data curation; Formal analysis; Funding acquisition; Investigation; Methodology; Project administration; Resources; Software; Supervision; Validation; Writing-review & editing. **Carl Robinson:** Conceptualisation; Data curation; Formal analysis; Funding acquisition; Investigation; Methodology; Project administration; Resources; Software; Supervision; Validation; Writing-review & editing. **Tom A. Jordan:** Data curation; Funding acquisition; Investigation; Project administration; Supervision; Validation; Writing-review & editing. **Paul V. Brennan:** Conceptualisation; Funding acquisition; Methodology; Project administration; Resources; Supervision; Writing-review & editing.

ACKNOWLEDGEMENTS

We thank K. Nicholls for the suggestions and reviews. This work has received funding from the NERC grant NE/L013444/1, project: Ice shelves in a warming world: Filchner Ice Shelf System (FISS), Antarctica. The 2016/17 data were collected as part of the NERC grant NE/L013770/1, project: Ice shelves in a warming world: Filchner Ice Shelf System (FISS), Antarctica. The 2019/20 data were collected as part of the BAS National Capability contribution to the NERC/NSF International Thwaites Glacier Collaboration (ITGC) program.

CONFLICT OF INTEREST STATEMENT

All authors confirm the originality of the work, agree with the terms and conditions of the submission, and declare there is no conflict of interest.

DATA AVAILABILITY STATEMENT

The calibration data, SAR images and DoA images that support the findings of this study are openly available in NERC EDS UK Polar Data Centre at <https://doi.org/10.5285/FAAC4156-047D-47BA-9E31-1A4F766BFDF8>, dataset ID GB/NERC/BAS/PDC/01708. The software scripts for reading the calibration data and representing the antenna patterns (Figures 2–3) are openly available in the BAS GitHub repository at <https://github.com/antarctica/calibration-processing-parameters-PASIN2.git>.

ORCID

Álvaro Arenas-Pingarrón  <https://orcid.org/0000-0001-9623-9937>

Tom A. Jordan  <https://orcid.org/0000-0003-2780-1986>

Paul V. Brennan  <https://orcid.org/0000-0002-3145-3868>

REFERENCES

1. Fretwell, P., et al.: Bedmap2: improved ice bed, surface and thickness datasets for Antarctica. *Cryosphere* 7, 375–393 (2013). <https://doi.org/10.5194/tc-7-375-2013>
2. MacGregor, J.A., et al.: Radiostratigraphy and age structure of the Greenland ice sheet. *J. Geophys. Res. Earth Surf.* 120(2), 212–241 (2015). <https://doi.org/10.1002/2014jf003215>

3. Morlighem, M., et al.: Deep glacial troughs and stabilizing ridges unveiled beneath the margins of the Antarctic ice sheet. *Nat. Geosci.* 13(2), 132–137 (2020). <https://doi.org/10.1038/s41561-019-0510-8>
4. Frémand, A.C., et al.: British Antarctic Survey's aerogeophysical data: releasing 25 years of airborne gravity, magnetic, and radar datasets over Antarctica. *Earth Syst. Sci. Data* 14(7), 3379–3410 (2022). <https://doi.org/10.5194/essd-14-3379-2022>
5. Evans, S., Smith, B.M.E.: A radio-echo equipment for depth sounding in polar ice sheets. *J. Phys. E Sci. Instrum.* 2(2), 131–136 (1969). <https://doi.org/10.1088/0022-3735/2/2/302>
6. Wu, X., et al.: Ice sheet bed mapping with airborne SAR tomography. *IEEE Trans. Geosci. Rem. Sens.* 49(10), 3791–3802 (2011). <https://doi.org/10.1109/tgrs.2011.2132802>
7. Rodriguez-Morales, F., et al.: Dual frequency and multi-receiver radars for sounding and imaging polar ice sheets. In: *Proc. 7th Eur. Conf. Synthetic Aperture Radar.* (2008)
8. Rodriguez-Morales, F., et al.: Advanced multifrequency radar instrumentation for polar research. *IEEE Trans. Geosci. Rem. Sens.* 52(5), 2824–2842 (2014). <https://doi.org/10.1109/tgrs.2013.2266415>
9. Wang, Z., et al.: Multichannel wideband synthetic aperture radar for ice sheet Remote sensing: development and the first deployment in Antarctica. *IEEE J. Sel. Top. Appl. Earth Obs. Rem. Sens.* 9(3), 980–993 (2016). <https://doi.org/10.1109/jstars.2015.2403611>
10. Dall, J., et al.: ESA'S POLarimetric airborne radar ice sounder (POLARIS): design and first results. *IET Radar, Sonar Navig.* 4(3), 488–496 (2010). <https://doi.org/10.1049/iet-rsn.2009.0035>
11. Nielsen, U., Dall, J.: Direction-of-Arrival estimation for radar ice sounding surface clutter suppression. *IEEE Trans. Geosci. Rem. Sens.* 53(9), 5170–5179 (2015). <https://doi.org/10.1109/tgrs.2015.2418221>
12. Paden, J., et al.: Ice-sheet bed 3-D tomography. *J. Glaciol.* 56(195), 3–11 (2010). <https://doi.org/10.3189/002214310791190811>
13. Hélicère, F., et al.: Radio echo sounding of pine Island glacier, west Antarctica: aperture synthesis processing and analysis of feasibility from space. *IEEE Trans. Geosci. Rem. Sens.* 45(8), 2573–2582 (2007). <https://doi.org/10.1109/tgrs.2007.897433>
14. Rose, K.C., et al.: Early East antarctic ice sheet growth recorded in the landscape of the gamburtsev subglacial mountains. *Earth Planet Sci. Lett.* 375, 1–12 (2013). <https://doi.org/10.1016/j.epsl.2013.03.053>
15. Jordan, T.A., et al.: Anomalously high geothermal flux near the South Pole. *Sci. Rep.* 8(1), 776–786 (2018). <https://doi.org/10.1038/s41598-018-35182-0>
16. Arenas-Pingarrón, A.: Calibration Processing Parameters PASIN2. BAS GitHub Repository (2022). last access: <https://github.com/antarctica/calibration-processing-parameters-PASIN2.git> 16 Dec 2022
17. Schmidt, R.: Multiple emitter location and signal parameter estimation. *IEEE Trans. Antenn. Propag.* 34(3), 276–280 (1986). <https://doi.org/10.1109/tap.1986.1143830>
18. Marple, S.L., Jr.: *Digital Spectral Analysis*, 2nd ed. Dover Publications, Mineola, NY (2019)
19. Proakis, J.G., Manolakis, D.G.: ch.12, sec.5. In: *Digital Signal Processing: Principles, Algorithms, and Applications*, 3rd ed. Prentice-Hall, Upper Saddle River (1996)
20. Dowdeswell, J.A., Evans, S.: Investigations of the form and flow of ice sheets and glaciers using radio-echo sounding. *Rep. Prog. Phys.* 67(10), 1821–1861 (2004). <https://doi.org/10.1088/0034-4885/67/10/r03>
21. Munson, D.C., Visentin, R.L.: A signal processing view of strip-mapping synthetic aperture radar. *IEEE Trans. Acoust. Speech Signal Process.* 37(12), 2131–2147 (1989). <https://doi.org/10.1109/29.45556>
22. Kusk, A., Dall, J.: SAR focusing of P-band ice sounding data using back-projection. In: *Proc. 2010 IEEE Int. Geosci. and Remote Sens. Symp.*, pp. 4071–4074. Honolulu (2010)
23. Yan, J.-B., et al.: Measurements of in-flight cross-track antenna patterns of radar depth sounder/imager. *IEEE Trans. Antenn. Propag.* 60(12), 5669–5678 (2012). <https://doi.org/10.1109/tap.2012.2211327>
24. Arenas Pingarrón, A., et al.: Airborne Synthetic Aperture Radar Ice-Sounding Depth Profiles from Recovery Ice Stream 2016/17, and Calibration Data from Rothera 2016/17 and 2019/20 (Version 1.0). NERC EDS UK Polar Data Centre (2023). <https://doi.org/10.5285/FAAC4156-047D-47BA-9E31-1A4F766BFDF8>
25. Burden, R.L., Faires, J.D.: Solutions of equations in one variable. In: *Numerical Analysis*, 8th ed, pp. 46–53. Thomson Brooks/Cole, Belmont (2005)
26. Castelletti, D., et al.: An interferometric approach to cross-track clutter detection in two-channel VHF radar sounders. *IEEE Trans. Geosci. Rem. Sens.* 55(11), 6128–6140 (2017). <https://doi.org/10.1109/tgrs.2017.2721433>
27. Pattyn, F.: The paradigm shift in Antarctic ice sheet modelling. *Nat. Commun.* 9(1), 2728 (2018). <https://doi.org/10.1038/s41467-018-05003-z>
28. Matsuoka, K., et al.: Quantarctica, an integrated mapping environment for Antarctica, the Southern Ocean, and sub-Antarctic islands. *Environ. Model. Software* 140, 105015 (2021). <https://doi.org/10.1016/j.envsoft.2021.105015>
29. Rignot, E., Mouginot, J., Scheuchl, B.: Ice flow of the Antarctic ice sheet. *Science* 333(6048), 1427–1430 (2011). <https://doi.org/10.1126/science.1208336>
30. Rignot, E., Mouginot, J., Scheuchl, B.: MEASURES InSAR-Based Antarctica Ice Velocity Map, Version 1. Boulder, Colorado USA: NASA EOSDIS Distributed Active Archive Center at NSIDC. Accessed on 4 Sept 2012. <https://doi.org/10.5067/MEASURES/CRYOSPHERE/nsidc-0484.001>
31. Corr, H., et al.: Processed Airborne Radio-Echo Sounding Data from the FISS 2016 Surveys Covering the Filchner and Halley Ice Shelves, and the English Coast (Western Palmer Land), West Antarctica (2016/2017) (Version 1.0). NERC EDS UK Polar Data Centre (2021). <https://doi.org/10.5285/0CB61583-3985-4875-B141-5743E68ABE35>
32. Le Brocq, A.M., et al.: Evidence from ice shelves for channelized melt-water flow beneath the Antarctic Ice Sheet. *Nat. Geosci.* 6(11), 945–948 (2013). <https://doi.org/10.1038/ngeo1977>

How to cite this article: Arenas-Pingarrón, Á., et al.: Polarimetric airborne scientific instrument, mark 2, an ice-sounding airborne synthetic aperture radar for subglacial 3D imagery. *IET Radar Sonar Navig.* 1–14 (2023). <https://doi.org/10.1049/rsn2.12428>